

# Phase transitions beyond post-perovskite in NaMgF<sub>3</sub> to 160 GPa

Rajkrishna Dutta<sup>a,1</sup>, Eran Greenberg<sup>b</sup>, Vitali B. Prakapenka<sup>b</sup>, and Thomas S. Duffy<sup>a</sup>

<sup>a</sup>Department of Geosciences, Princeton University, Princeton, NJ 08544; and <sup>b</sup>Center for Advanced Radiation Sources, University of Chicago, Chicago, IL 60637

Edited by Ho-Kwang Mao, Center for High Pressure Science and Technology Advanced Research, Shanghai, China, and approved August 8, 2019 (received for review June 4, 2019)

Neighborite, NaMgF<sub>3</sub>, is used as a model system for understanding phase transitions in ABX<sub>3</sub> systems (e.g., MgSiO<sub>3</sub>) at high pressures. Here we report diamond anvil cell experiments that identify the following phases in NaMgF<sub>3</sub> with compression to 162 GPa: NaMgF<sub>3</sub> (perovskite) → NaMgF<sub>3</sub> (post-perovskite) → NaMgF<sub>3</sub> (Sb<sub>2</sub>S<sub>3</sub>-type) → NaF (B2-type) + NaMg<sub>2</sub>F<sub>5</sub> ( $P2_1/c$ )  $\rightarrow$  NaF (B2) + MgF<sub>2</sub> (cotunnitetype). Our results demonstrate the existence of an Sb<sub>2</sub>S<sub>3</sub>-type postpost-perovskite ABX<sub>3</sub> phase. We also experimentally demonstrate the formation of the P21/c AB2X5 phase which has been proposed theoretically to be a common high-pressure phase in ABX<sub>3</sub> systems. Our study provides an experimental observation of the full sequence of phase transitions from perovskite to post-perovskite to post-post-perovskite followed by 2-stage breakdown to binary compounds. Notably, a similar sequence of transitions is predicted to occur in MgSiO<sub>3</sub> at ultrahigh pressures, where it has implications for the mineralogy and dynamics in the deep interior of large, rocky extrasolar planets.

post-post-perovskite | high pressure | analog

gSiO<sub>3</sub> perovskite (bridgmanite, Pv, *Pbnm*) is expected to be the most abundant mineral in the Earth's lower mantle. At pressure and temperature conditions (~125 GPa, >2,000 K) of the lowermost ~150 km of the mantle (D" layer), bridgmanite undergoes a phase transition into the CaIrO<sub>3</sub>-type structure (Cmcm) known as post-perovskite (1, 2) (pPv). Although pPv is expected to be the final ABO3 silicate phase in the Earth's interior, additional higher pressure "post-post-perovskite" (ppPv) phases may play an important role in the interiors of large terrestrial exoplanets (3, 4). Recent advances in astronomy have led to discoveries of many large rocky planets up to ~10 Earth masses in size (5). These exoplanets are expected to have very high internal pressures and temperatures (up to ~4,000 GPa, ~10,000 K). Laboratory experiments attempting to replicate such conditions are extremely challenging and generally beyond the reach of even state-of-the-art experimental techniques for static compression. Our understanding of the mineralogy of rocky exoplanets is therefore based largely on quantum mechanical computations, but these require experimental verification. One approach to testing the theoretical results is to compare analog materials that display a similar sequence of phase transitions as expected in silicate minerals but at lower pressures.

NaMgF<sub>3</sub> (neighborite) is both isostructural and isoelectronic to bridgmanite, crystallizing in the orthorhombic Pv (Pbnm) structure at ambient conditions. Neighborite undergoes a pressureinduced phase transition to the pPv structure at pressures as low as 19 GPa at room temperature (6) (compared to ~125 GPa, 2,000 K in MgSiO<sub>3</sub>). Based on comparison of structural parameters (e.g., axial ratios, polyhedral volume, octahedral tilt, etc.) of several analogs, it was concluded that NaMgF3 pPv is likely an excellent analog for MgSiO<sub>3</sub> pPv (6-8) (SI Appendix,

Earlier theoretical calculations on MgSiO<sub>3</sub> pPv predict a 2-stage (9) dissociation process under compression as follows:

$$\begin{split} \text{MgSiO}_3\text{pPv} &\rightarrow \text{MgSi}_2\text{O}_5 \left(\text{P2}_1/c\text{-type}\right) \\ &+ \text{CsCl-type MgO} \left(0.9 \text{ TPa}\right) \\ &\rightarrow \text{Fe}_2\text{P-type SiO}_2 \left(\text{P$\bar{6}$2$m}\right) \\ &+ \text{CsCl-type MgO} \left(2.1 \text{ TPa}\right). \end{split}$$

A more recent update (4) supports a 3-step breakdown:

$$\begin{split} \text{MgSiO}_3\text{pPv} &\rightarrow \text{Mg}_2\text{SiO}_4 \, (I\bar{4}2\text{d-type}) + \text{MgSi}_2\text{O}_5 \, (0.75 \text{ TPa}) \\ &\rightarrow \text{Mg}_2\text{SiO}_4 \, (I\bar{4}2\text{d-type}) + \text{Fe}_2\text{P-type SiO}_2 \, (1.31 \text{ TPa}) \\ &\rightarrow \text{Fe}_2\text{P-type SiO}_2 + \text{CsCl-type MgO} \, (3.1 \text{ TPa}). \end{split}$$

Another computational study (10) has instead proposed a temperature-dependent 3-stage dissociation pathway. At relatively low temperatures (<6,400 K), the above sequence (Eq. 2) is followed. Under higher temperatures (>6,600 K), MgSiO<sub>3</sub> pPv is predicted to instead decompose into Mg2SiO4 and MgSi2O5, followed by decomposition of Mg<sub>2</sub>SiO<sub>4</sub> into MgO and MgSi<sub>2</sub>O<sub>5</sub> and finally into the simple oxides. Current experiments (11) on MgSiO<sub>3</sub> extending up to 265 GPa find that the pPv phase remains stable to this pressure and none of the proposed higher-pressure phases have yet been observed experimentally.

In the case of pPv NaMgF<sub>3</sub>, a 2-stage dissociation (12) analogous to Eq. 1 has been proposed: from pPv into NaMg<sub>2</sub>F<sub>5</sub>  $(P2_1/c$ -type) + B2-NaF (29 GPa) and then into B2-NaF + cotunnite-MgF<sub>2</sub> (71 GPa). Additional ppPv ABX<sub>3</sub> structures that have also been proposed theoretically in this system include an

#### **Significance**

The high-pressure behavior of NaMgF<sub>3</sub> is of interest due to its role as a low-pressure analog for phase transitions in the MgSiO<sub>3</sub> system. In this work, we have used the diamond anvil cell and synchrotron X-ray diffraction techniques to study structural transitions in NaMgF3 to 1.6 Mbars. Our work has identified a sequence of high-pressure phases beyond postperovskite in this ABX<sub>3</sub> system. We report the presence of a post-post-perovskite phase, followed by a partial and then complete dissociation into binary fluorides. A similar sequence of high-pressure phase transitions in MgSiO<sub>3</sub> at very high pressure-temperature conditions has implications for understanding the interiors of large rocky exoplanets.

Author contributions: R.D. and T.S.D. designed research; R.D. and T.S.D. performed research; E.G. and V.B.P. contributed new reagents/analytic tools; R.D. analyzed data; and R.D. and T.S.D. wrote the paper.

The authors declare no conflict of interest.

This article is a PNAS Direct Submission.

Published under the PNAS license

<sup>1</sup>To whom correspondence may be addressed. Email: rd7@princeton.edu.

This article contains supporting information online at www.pnas.org/lookup/suppl/doi:10. 1073/pnas.1909446116/-/DCSupplemental.

 $La_2S_3$ -type (*Pnma*, 51 GPa, ref. 13), an  $Sb_2S_3$ -type (*Pnma*, 44 GPa, ref. 14), and a  $P6_3/mmc$ -type (223 GPa, ref. 14) structure. The  $La_2S_3$ -type ppPv phase was predicted to be stable not only in NaMgF3 but also in a wide range of ABX3 compounds, with the notable exception of MgSiO3 (13). However, both the  $La_2S_3$ - and  $Sb_2S_3$ -type phases were found to be energetically unfavorable with respect to NaF + MgF2 above 48 GPa (15).

In the ABX<sub>3</sub> pPv structure (Cmcm), BX<sub>6</sub> octahedra share edges and corners and form layers oriented perpendicular to the most-compressible b axis. With increasing compression, X anions enter the primary coordination polyhedra of B cations in the octahedral sheets. This increases the B coordination number to 7 and links alternating pairs of edge-sharing, 8-fold-coordinated Mg-polyhedra leading to the Sb<sub>2</sub>S<sub>3</sub>-type structure (Pmcn setting). The AB<sub>2</sub>X<sub>5</sub> ( $P2_1/c$ -type) structure is also of interest as a possible decomposition product of ABX<sub>3</sub> compounds (9). In AB<sub>2</sub>X<sub>5</sub>, there are 2 types of B atoms, one 7-coordinated and the other 8-coordinated, while the coordination of the A cation also increases to 9. The  $P2_1/c$ -AB<sub>2</sub>X<sub>5</sub> structure may occur commonly at high pressures (9).

In addition to NaMgF<sub>3</sub>, pPv and ppPv phases have been synthesized in related compositions with transition elements (e.g., Fe, Ni, and Co) substituting for Mg in the B site (16, 17). These compounds show varied high-pressure behavior. In NaFeF<sub>3</sub>, a transition from the pPv phase to the Sb<sub>2</sub>S<sub>3</sub>-type structure has been reported at 22 GPa (16). NaCoF<sub>3</sub> pPv dissociated into a mixture of unknown, unquenchable phases on laser heating above 26 GPa (17), while no disproportionation or phase transition of pPv was observed in NaNiF<sub>3</sub> at least up to 54 GPa (17).

The search for ppPv phases has also extended to oxide systems including FeSiO<sub>3</sub>, FeGeO<sub>3</sub>, MnTiO<sub>3</sub>, and FeTiO<sub>3</sub>. In the case of both FeSiO<sub>3</sub> (18) and FeGeO<sub>3</sub> (19), neither Pv nor pPv phases are observed and a mixture of FeO + SiO<sub>2</sub>/GeO<sub>2</sub> is stable at least up to 149 and 127 GPa, respectively. In MnTiO<sub>3</sub>, the Pv phase was found to decompose into MnO + MnTi<sub>2</sub>O<sub>5</sub> above 38 GPa (20). Several decomposition pathways (21–23) have been proposed for FeTiO<sub>3</sub>, but no pPv or ppPv phases have been observed. Both MnTi<sub>2</sub>O<sub>5</sub> and FeTi<sub>2</sub>O<sub>5</sub> were reported to have orthorhombic (20, 23) symmetry, but the structure is not known. The *P2*<sub>1</sub>/*c*-type AB<sub>2</sub>X<sub>5</sub> structure, although monoclinic, has only a small monoclinic distortion from an orthorhombic cell and may account for these structures (9).

In this work, the high-pressure behavior of NaMgF<sub>3</sub>, a low-pressure analog of MgSiO<sub>3</sub>, was examined to explore the stability of phases beyond pPv. Laser-heated diamond anvil cell experiments coupled with synchrotron X-ray diffraction (Xrd) techniques were applied. We show that pPv NaMgF<sub>3</sub> undergoes multiple pressure-induced phase transitions and eventually decomposes into a mixture of binary fluorides.

#### Results

In the first experimental run (Exp. 1; SI Appendix, Table S2), room-temperature Xrd patterns were collected on an NaMgF<sub>3</sub> sample at several compression steps up to a peak pressure of 87 GPa (Fig. 1). At 13 GPa, the diffraction pattern can be indexed using the Pv structure in agreement with previous studies (24) (SI Appendix, Fig. S1). The measured unit cell volume of 199.8 (2) Å<sup>3</sup> at this pressure is consistent with that reported by Hustoft et al. (24) (198.1 Å<sup>3</sup> at 13 GPa). Upon further compression to 40 GPa, the diffraction pattern changed, indicating a pressureinduced phase transition. The observed pattern (SI Appendix, Fig. S2) is consistent with the CaIrO<sub>3</sub>-type pPv structure. Our measured cell volume [167.2 (2) Å<sup>3</sup>] is slightly higher than the expected volume based on the equation of state (EOS) parameters reported in an earlier study (24) (163.8 Å<sup>3</sup> at 40 GPa). It should be noted that the present experiment used no pressuretransmitting medium, whereas argon was used as a medium in the

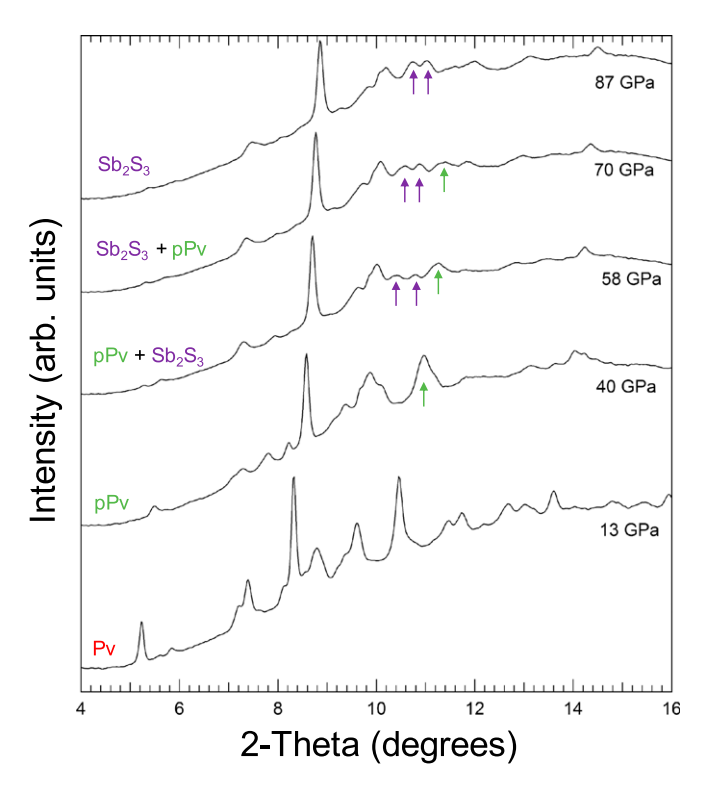


Fig. 1. Xrd patterns of NaMgF<sub>3</sub> compressed at room temperature. Green and purple arrows indicate the positions of the pPv (004), (113), (132) and Sb<sub>2</sub>S<sub>3</sub>-type (013), (311) peaks, respectively. See *Sl Appendix* for further details on peak identification.

previous work. A pressure medium was not used here in order to maximize the signal from the weakly scattering sample at higher pressures.

At 58 GPa, the diffraction pattern can no longer be indexed solely using the pPv structure (SI Appendix, Fig. S3). With increasing pressure, the intensity of the pPv peaks (004, 113, and 132; indicated by green arrow in Fig. 1) decreases and new peaks (indicated by purple arrows) grow near 2-theta of 10 to 11°. At ~87 GPa, the observed spectrum no longer shows any evidence of the pPv peaks and the new peaks identified previously are now the most intense peaks of the pattern, indicating the presence of a new phase. We attempted to index the diffraction pattern using the theoretically proposed La<sub>2</sub>S<sub>3</sub>-type (13) and Sb<sub>2</sub>S<sub>3</sub>-type (14) structures, using the theoretically determined structures as starting models. The Sb<sub>2</sub>S<sub>3</sub>-type structure can explain all of the major peaks in the observed pattern, while the former cannot. The appearance of the Sb<sub>2</sub>S<sub>3</sub>-type structure beginning from around 58 GPa is consistent with theoretical predictions (14, 15). Under further compression at room temperature, this phase was found to remain stable up to at least 160 GPa.

Computational studies predict that while the  $Sb_2S_3$ -type phase may have lower energy than pPv, it would still be unstable with respect to  $MgF_2 + NaF$  at all pressures (14, 15), suggesting that the phase that we observed may be metastable. In the next runs, we directly compressed the sample to 90 GPa (Exp. 2a, with Ne) and 87 GPa (Exp. 2b, without Ne) and heated it to peak temperatures of ~1,810 K and ~2,710 K for ~30 and ~20 min, respectively. Fig. 2 (Exp. 2a) and *SI Appendix*, Fig. S4 show the diffraction pattern obtained on quenching the sample after heating to 1,810 K (temperature-quenched pressure [P] = 91 GPa). It can be seen that the  $Sb_2S_3$ -type phase remains stable even after prolonged laser heating. Our experiments thus indicate that the  $Sb_2S_3$ -type phase is likely stable with respect to breakdown at these conditions and not a metastable phase.

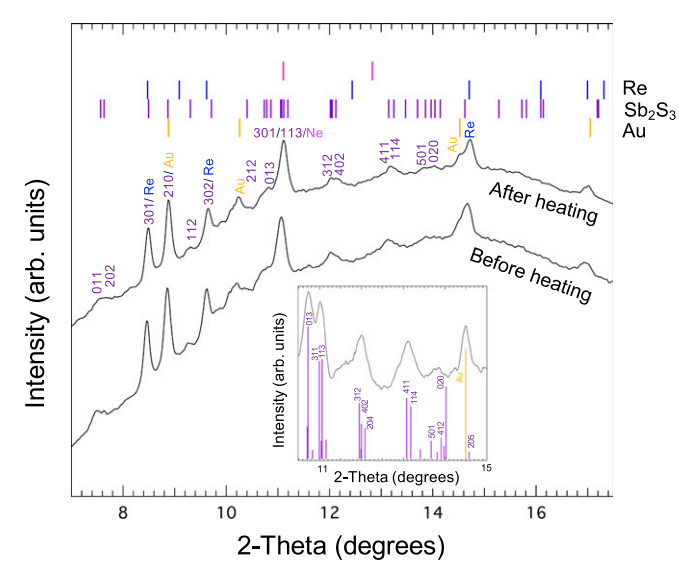


Fig. 2. Xrd pattern obtained before and after heating NaMgF $_3$  at  $\sim$ 1,810 K and 90 GPa followed by quenching to room temperature (quenched P = 91 GPa). The ticks at the top indicate Sb $_2$ S $_3$ -type NaMgF $_3$  (purple), Re (blue), Ne (pink), and Au (yellow) peaks, respectively. (*Inset*) A magnified view of a diffraction pattern (87 GPa) obtained in a separate run (unheated) conducted without Ne medium because Ne (111) overlaps with (311) and (113) peaks from the Sb $_2$ S $_3$ -type phase. Atomic positions from the theoretical calculations were used for calculating the intensities of the diffraction peaks in the inset.

Fig. 3 shows the pressure–volume behavior of the pv, pPv, and Sb<sub>2</sub>S<sub>3</sub>-type phases of NaMgF<sub>3</sub> based on this and previous work (see SI Appendix, Fig. S5 for the variation of lattice parameters with pressure). Using a third-order Birch-Murnaghan EOS fit to the data (Sb<sub>2</sub>S<sub>3</sub>-type), the resulting parameters are  $V_0 = 214$  (9) Å<sup>3</sup>,  $K_0 = 88$  (16) GPa, and  $K'_0 = 4$  (fixed), where V, K, and K' are the unit cell volume, bulk modulus, and its pressure derivative, respectively; the subscript 0 indicates ambient-pressure conditions. These values are consistent with the results of theoretical calculations (15)  $[V_0 = 218.7(3) \text{ Å}^3, K_0 = 78(4) \text{ GPa, and } K'_0 = 4.3].$ The EOS parameters are also comparable with those reported (24) for the Pv [ $V_0 = 225$ . 1 Å<sup>3</sup>,  $K_0 = 81$  (4) GPa, and  $K'_0 = 3.6$  (4)] and pPv phases [ $V_0 = 223$  Å<sup>3</sup>,  $K_0 = 54$  (3) GPa, and  $K'_0 = 5.7$  (4)]. Our EOS results suggest the transition from pPv to Sb<sub>2</sub>S<sub>3</sub>-type structure will have a small (~0.5%) volume change (at 55 GPa), which is less than the corresponding decrease in volume  $(\sim 4\%)$  at  $\sim 28$  GPa during the Pv-to-pPv transition (25). The small volume change is consistent with observations of the same transition in NaFeF3 at 22 GPa, where no detectable volume change was reported (16). However, it should be noted that these pressure-volume measurements were performed in absence of a pressure-transmitting medium and/or without laser annealing. Further experiments are necessary for more accurate determination of the EOS parameters of this phase.

In Exp. 2b, the sample was again compressed to near 90 GPa, but in this case the heating extended to higher temperatures. New diffraction peaks appeared after heating to ~2,590 K for ~5 min. The new peaks were retained on quenching to ambient temperature (quenched P = 88 GPa; Fig. 4). The most marked difference between the 2 patterns in Exps. 2a and 2b is the presence of the strong peak at  $2\theta = 11.38^{\circ}$ . The peak is consistent with the (110) reflection of NaF in the B2-type (cesium chloride) structure. The measured unit cell volume of CsCl-type NaF (54.19 ų) at 88 GPa is in reasonable agreement with predictions from a theoretical EOS (15) (55.4 ų). The presence of an NaF peak in our diffraction pattern suggests the sample has

dissociated into a phase assemblage such as NaMg<sub>2</sub>F<sub>5</sub> + NaF as predicted by theoretical calculations (12). This phase mixture is indeed consistent with the observed diffraction pattern (Fig. 4). The differences between the calculated and observed d-spacings for peaks of the NaMg<sub>2</sub>F<sub>5</sub> phase are <0.002 Å, indicating a good fit to the structure (SI Appendix, Table S4). The difference between the results of Exps. 2a and 2b can be explained in 2 ways. One possibility is that the Sb<sub>2</sub>S<sub>3</sub>-type phase is stable at relatively lower temperatures and dissociates into NaMg<sub>2</sub>F<sub>5</sub> + NaF at higher temperatures. Alternatively, high temperatures may be required to overcome the kinetic barrier for the transition and the Sb<sub>2</sub>S<sub>3</sub>-type structure is instead a metastable phase. We consider the former to be more likely given that the Sb<sub>2</sub>S<sub>3</sub>-type phase remained stable for nearly 30 min of heating at moderately high temperatures, but further studies at high temperature are needed.

In the next experiment (Exp. 3, no pressure medium), the sample was directly compressed to 134 GPa and then laser-heated. The diffraction pattern obtained on quenching the sample to room temperature after heating to ~2,600 K at 134 GPa (quenched P = 137 GPa) can also be indexed using NaMg<sub>2</sub>F<sub>5</sub> + NaF (*SI Appendix*, Fig. S6; see *SI Appendix* for detailed discussion). In the absence of experimental/theoretical data on unit cell parameters of NaMg<sub>2</sub>F<sub>5</sub> at high pressure, direct comparisons of lattice parameters with literature data are not possible. However, the experimental unit cell dimensions are in fair agreement with our theoretical calculations (*SI Appendix*, Fig. S4). The unit cell volume of NaF (48.8 ų) at 137 GPa is consistent with the prediction of a theoretically calculated EOS (15) (49.7 ų) at this pressure.

In the fourth run (Exp. 4), the sample was compressed directly to 162 GPa at room temperature. The sample was then heated

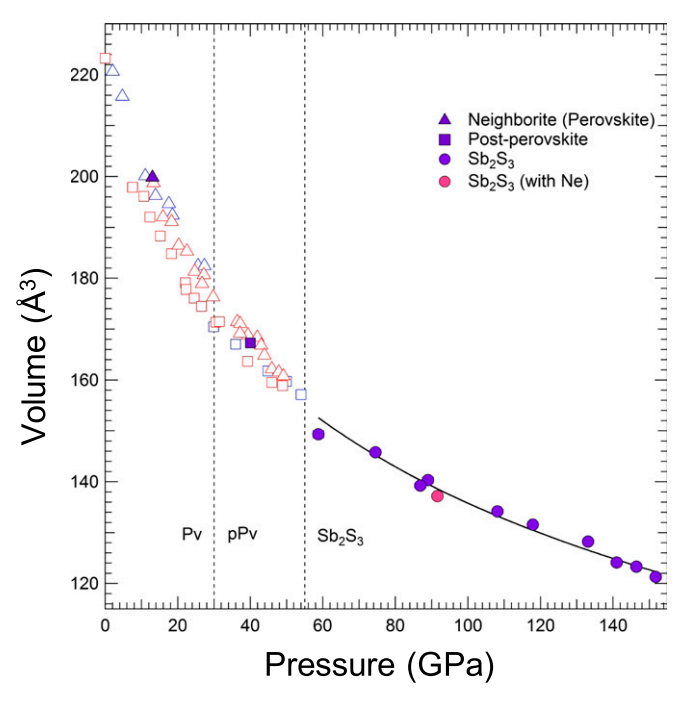


Fig. 3. Pressure variation of unit cell volume for Pv (triangles), pPv (squares), and  $Sb_2S_3$ -type (circles) phases of NaMgF3 at ambient temperature. Solid and open symbols represent this study (purple) and literature data (red, ref. 24. and blue, ref. 25), respectively. The pink symbol shows the volume of the  $Sb_2S_3$ -type phase compressed in a neon pressure-transmitting medium and quenched after laser heating. The solid black line is Birch–Murnaghan EOS fit to the  $Sb_2S_3$ -type phase (excluding the pink datum). The dashed black lines indicate the pv–pPv and pPv– $Sb_2S_3$  phase boundaries (15, 25).

Dutta et al. PNAS Latest Articles | 3 of 6

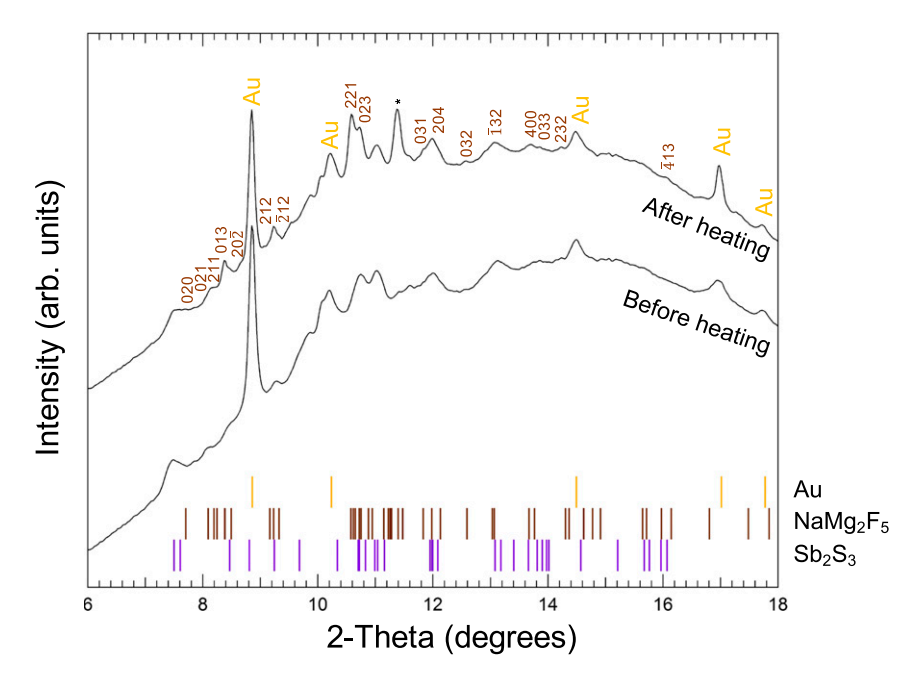


Fig. 4. Xrd pattern before and after heating NaMgF<sub>3</sub> to  $\sim$ 2,700 K at 87 GPa (quenched P after heating = 88 GPa). The ticks at the bottom indicate diffraction peaks positions of Sb<sub>2</sub>S<sub>3</sub>-type NaMgF<sub>3</sub> (purple), NaMg<sub>2</sub>F<sub>5</sub> (brown), and Au (yellow), respectively. Miller indices of the NaMg<sub>2</sub>F<sub>5</sub> peaks are listed above the observed pattern. An asterisk indicates the (110) peak of NaF in the CsCl-type structure.

for 20 min to a peak temperature of ~2,260 K, with the temperature being increased steadily during the heating cycle. New diffraction peaks appeared at  $\sim$ 1,830 K (in situ P = 172 GPa; Fig. 5) and were retained upon temperature quench. The Xrd pattern can be indexed using a mixture of cotunnite-type MgF2 and CsCl-type NaF. The difference between the observed and calculated d-spacings of the cotunnite-type phase of MgF<sub>2</sub> was less than 0.005 Å (SI Appendix, Table S6), indicating a good fit between the two. The unit cell volumes of cotunnite-type MgF<sub>2</sub> (69. 9 Å<sup>3</sup>) and CsCl-type NaF (46.9 Å<sup>3</sup>) are consistent with the respective volumes predicted from the EOS reported in previous experiments (15) (MgF<sub>2</sub> = 69.1 Å<sup>3</sup>, NaF = 47.8 Å<sup>3</sup> at 160 GPa). An additional peak of unknown origin at  $2\theta = 9.75^{\circ}$  (marked by an asterisk in Fig. 5) was observed. The peak may be due to formation of gold fluoride (Au<sub>2</sub>F) as predicted from theoretical calculations (26) (see SI Appendix, section S5 for details). The same

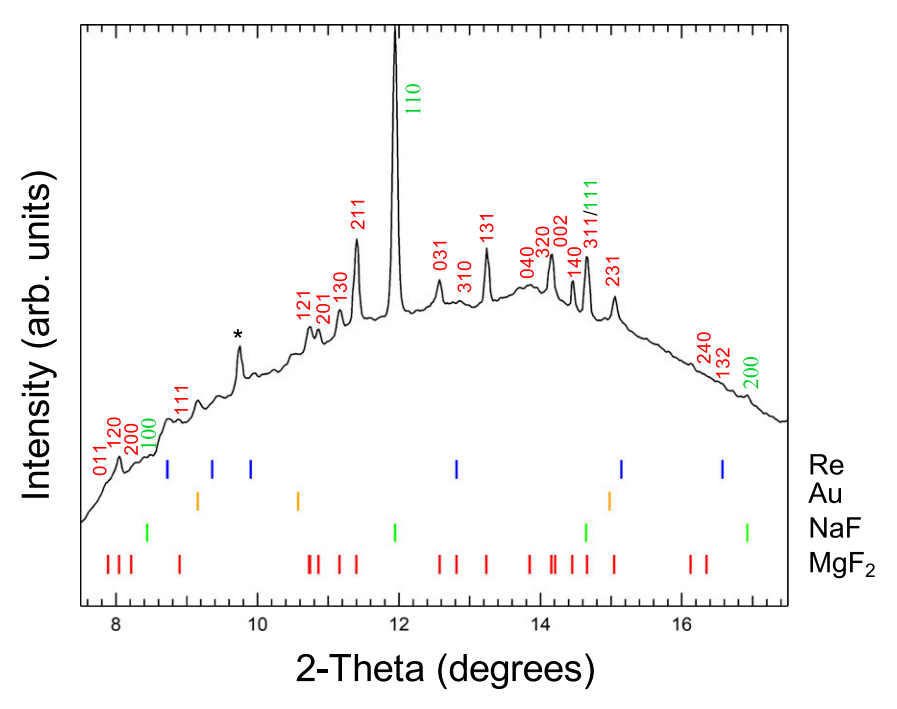


Fig. 5. Xrd pattern obtained on heating NaMgF<sub>3</sub> to 1,830 K at 160 GPa (in situ P = 172 GPa). The ticks at the bottom indicate cotunnite-type MgF<sub>2</sub> (red), NaF-B2 (green), Re (blue), and Au (yellow), respectively. An asterisk indicates an unindexed peak (SI Appendix).

phase transition from  $Sb_2S_3$  to  $MgF_2$  and NaF was also observed in an additional experiment (Exp. 5) for a sample that was directly compressed to 150 GPa and then heated to  $\sim 2,200$  K.

#### Discussion

The high-pressure transition pathways of pPv phases are of interest for understanding the possible mineralogy and evolution of super-Earth planets. Dissociation of pPv is important for understanding mantle convection in large, rocky exoplanets (27). Dissociation transitions (4) may affect layering and viscosity which will, in turn, affect heat flow and long-term thermal evolution. Thus, an understanding of such transitions in pPv materials is fundamentally important for developing plausible evolutionary models for super-Earths.

Because of the extremely high-pressure and -temperature conditions necessary for the ppPv phase transitions in MgSiO<sub>3</sub>, our understanding of these transitions is entirely based on theoretical calculations (4, 9, 10). While laser-driven dynamic ramp compression techniques combined with Xrd (28) can reach pressures close to the terapascal range, such methods are generally limited to high-symmetry and/or high-atomic-number solids at present. To probe the ppPv phases, static experimental studies in the diamond anvil cell have focused on analog compounds which display lower transition pressures compared to MgSiO<sub>3</sub>. In the case of oxides, experiments have not identified direct analogs for the expected transition sequence in MgSiO<sub>3</sub>. In MgGeO<sub>3</sub>, the pPv phase is experimentally observed up to 200 GPa (29). ABO<sub>3</sub> oxides with transition elements in the A site such as FeSiO<sub>3</sub> (18), FeGeO<sub>3</sub> (19), MnTiO<sub>3</sub> (20), and FeTiO<sub>3</sub> (22) do not exhibit either the Pv and/or the pPv phase.

NaMgF<sub>3</sub>, on the other hand, is a very good structural analog for both the Pv and pPv phases of MgSiO<sub>3</sub> (7, 30) (*SI Appendix*, Table S1). Fig. 6 shows a schematic phase diagram of the NaMgF<sub>3</sub> system summarizing available experimental data. Based on our study, the observed phase transition sequence in NaMgF<sub>3</sub> neighborite is

$$Pv \rightarrow pPv \rightarrow Sb_2S_3$$
-type  $\rightarrow NaMg_2F_5 + NaF \rightarrow NaF + MgF_2$ .

Although this is in many respects consistent with theoretical predictions (12, 15), there are important differences. As previously mentioned, the Sb<sub>2</sub>S<sub>3</sub>-type phase is predicted to be metastable, while our experiments indicate it may be a stable ppPv phase at low to moderate temperatures. Our study provides experimental evidence for a 2-stage dissociation of a pPv-forming ABX<sub>3</sub> compound. We also provide experimental evidence for formation of P2<sub>1</sub>/c-type NaMg<sub>2</sub>F<sub>5</sub>, a structure type that has been proposed to be a common high-pressure form in AB<sub>2</sub>X<sub>5</sub>-type compounds at high pressures (12). Our work also confirms the theoretical predictions (4, 9, 10, 12) that a mixture of  $AX + BX_2$  is the final product of  $ABX_3$  systems. However, our experiments show that the binary fluorides are stabilized only above ~150 GPa, which is much higher than the theoretically predicted transition pressure [71 GPa (12) or 48 GPa (15)].

The dissociation transitions in MgSiO<sub>3</sub> are predicted to have large negative Clapeyron slopes (9), which would promote stratification in the mantles of super-Earth planets (27, 31). The transitions to a Sb<sub>2</sub>S<sub>3</sub>-type ppPv phase, on the other hand, may only have minor effects on dynamic behavior due to the very small volume change. Other pressure- and temperature-dependent properties like viscosity may dramatically change across phase transitions, which could also significantly affect the mantle dynamics. The high-pressure behavior of NaMgF<sub>3</sub> is important as an analog system for understanding possible phase transitions and their effects in the interiors of super-Earths.

#### Methodology

NaMgF $_3$  Pv starting material was synthesized by heating stoichiometric proportions of NaF and MgF $_2$ . The powdered sample was mixed with 10 wt % Au as a pressure calibrant and loaded into symmetric diamond anvil cells with 75- to 200- $\mu$ m-diameter culets. Samples were compressed up to a peak pressure

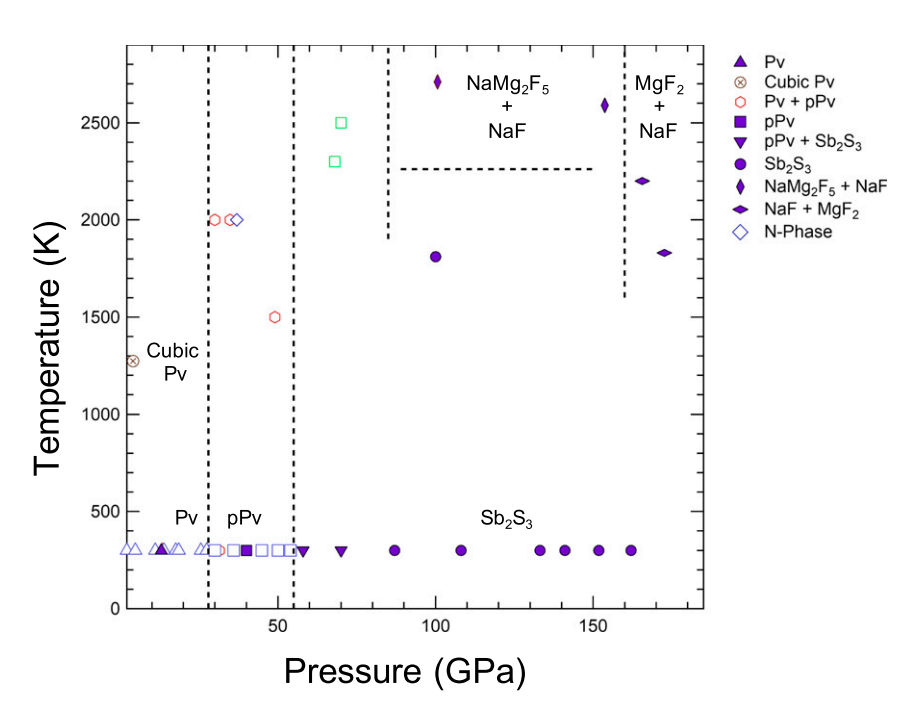


Fig. 6. Summary of constraints on the high-pressure and -temperature phase diagram of NaMgF<sub>3</sub>. The solid symbols (triangles: Pv, star: pPv, circles:  $Sb_2S_3$ , inverted triangle:  $pPv + Sb_2S_3$ , vertical diamonds: NaMg<sub>2</sub>F<sub>5</sub> + NaF, horizontal diamonds: NaF + MgF<sub>2</sub>) represent the present experimental data. Open symbols (red, ref. 24; blue, ref. 25; and green, ref. 32) show experimental literature data for the respective phases. The brown open circle indicates the high-temperature cubic phase (33, 34). The dashed black lines are schematic phase boundaries.

Dutta et al. PNAS Latest Articles | 5 of 6

of 160 GPa. Double-sided pulsed-laser heating was used to heat the sample up to ~2,700 K and temperatures were measured by spectroradiometry. Angle-dispersive synchrotron Xrd was carried out at beamline 13-ID-D of the Advanced Photon Source using a monochromatic X-ray beam ( $\lambda = 0.3344 \text{ Å}$ ) focused to dimensions of  ${\sim}3~\mu\text{m} \times 3~\mu\text{m}$  with Kirkpatrick–Baez mirrors. A 2D charge-coupled device (Mar165) or a CdTe 1M Pilatus detector was used to collect the diffraction patterns. The Xrd patterns were fit using backgroundsubtracted Voigt line shapes. Lattice parameters were calculated by leastsquares refinement of the fitted peak position. LeBail refinements were carried out on selected data using the programs GSAS/EXPGUI. Further details are provided in SI Appendix, section S2.

- 1. A. R. Oganov, S. Ono, Theoretical and experimental evidence for a post-perovskite phase of MgSiO<sub>3</sub> in Earth's D" layer. Nature 430, 445-448 (2004).
- 2. M. Murakami, K. Hirose, K. Kawamura, N. Sata, Y. Ohishi, Post-perovskite phase transition in MgSiO3. Science 304, 855-858 (2004).
- 3. T. Duffy, N. Madhusudhan, K. K. M. Lee, "2.07-Mineralogy of super-earth planets" in
- Treatise on Geophysics, G. Schubert, Ed. (Elsevier, Oxford, ed. 2, 2015), pp. 149-178. 4. K. Umemoto et al., Phase transitions in MgSiO<sub>3</sub> post-perovskite in super-Earth mantles. Earth Planet. Sci. Lett. **478**, 40–45 (2017).
- G. W. Marcy et al., Occurrence and core-envelope structure of 1-4× Earth-size planets around Sun-like stars. Proc. Natl. Acad. Sci. U.S.A. 111, 12655-12660 (2014).
- 6. H.-Z. Liu et al., Octahedral tilting evolution and phase transition in orthorhombic NaMgF<sub>2</sub> perovskite under pressure, Geophys, Res. Lett. 32, L04304 (2005).
- 7. T. S. Duffy, Some recent advances in understanding the mineralogy of Earth's deep mantle. Philos. Trans. A Math. Phys. Eng. Sci. 366, 4273-4293 (2008).
- 8. K. Umemoto, R. M. Wentzcovitch, D. J. Weidner, J. B. Parise, NaMgF<sub>3</sub>: A low-pressure analog of MgSiO<sub>3</sub>. Geophys. Res. Lett. 33, L15304 (2006).
- K. Umemoto, R. M. Wentzcovitch, Two-stage dissociation in MgSiO<sub>3</sub> post-perovskite. Earth Planet. Sci. Lett. 311, 225-229 (2011).
- 10. H. Niu, A. R. Oganov, X.-Q. Chen, D. Li, Prediction of novel stable compounds in the Ma-Si-O system under exoplanet pressures, Sci. Rep. 5, 18347 (2015).
- 11. T. Sakai, H. Dekura, N. Hirao, Experimental and theoretical thermal equations of state of MgSiO<sub>3</sub> post-perovskite at multi-megabar pressures. Sci. Rep. 6, 22652 (2016).
- 12. K. Umemoto, R. M. Wentzcovitch, "Two-stages dissociation of NaMgF<sub>3</sub> postperovskite: A potential low-pressure analog of MgSiO<sub>3</sub> at multi-Mbar pressures" in Proceedings of the International Symposium "Nanoscience and Quantum Physics" 2012 (Physical Society of Japan, 2015) vol. 4,011002.
- 13. C. Xu et al., Prediction of a stable post-post-perovskite structure from first principles. Phys. Rev. B 91, 020101 (2015).
- K. Umemoto, R. M. Wentzcovitch, Potential ultrahigh pressure polymorphs of ABX<sub>3</sub>type compounds. Phys. Rev. B 74, 224105 (2006).
- C. Jakymiw et al., The phase diagrams of KCaF<sub>3</sub> and NaMgF<sub>3</sub> by ab initio simulations. Phys. Chem. Miner. 45, 311-322 (2018).
- 16. W. A. Crichton, F. L. Bernal, J. Guignard, M. Hanfland, S. Margadonna, Observation of Sb<sub>2</sub>S<sub>3</sub>-type post-post-perovskite in NaFeF<sub>3</sub>. Implications for ABX<sub>3</sub> and A<sub>2</sub>X<sub>3</sub> systems at ultrahigh pressure, Mineral, Mag. 80, 659-674 (2016).
- 17. H. Yusa et al., Perovskite-to-postperovskite transitions in NaNiF<sub>3</sub> and NaCoF<sub>3</sub> and disproportionation of NaCoF<sub>3</sub> postperovskite under high pressure and high temperature. Inorg. Chem. 51, 6559-6566 (2012).

ACKNOWLEDGMENTS. We thank S. J. Tracy, C. V. Stan, C. E. White, J. K. Wicks, R. J. Cava, C. Prescher, and S. Tkachev for assistance with experiments and theoretical calculations and G. Yang for valuable discussion. The work was funded by NSF Grants EAR-1644614 and EAR-1836852. We acknowledge use of the Advanced Photon Source, an Office of Science User Facility, US Department of Energy (DOE) under Contract DE-AC02-06CH11357. GeoSoilEnviroCARS (GSECARS, Sector 13) is supported by NSF Earth Sciences Grant EAR-1634415 and the DOE Geosciences Grant DE-FG02-94ER14466. The gas-loading facility at GSECARS is partially supported by the Consortium for Materials Properties Research in Earth Sciences under NSF Cooperative Agreement EAR-1606856.

- 18. K. Fujino et al., Stability of the perovskite structure and possibility of the transition to the post-perovskite structure in CaSiO<sub>3</sub>, FeSiO<sub>3</sub>, MnSiO<sub>3</sub> and CoSiO<sub>3</sub>. Phys. Earth Planet. Inter. 177, 147-151 (2009)
- 19. R. Dutta et al., Phase stability of iron germanate, FeGeO<sub>3</sub>, to 127 GPa. Phys. Chem. Miner. 45, 367-379 (2018).
- 20. T. Okada, T. Yagi, D. Nishio-Hamane, High-pressure phase behavior of MnTiO<sub>3</sub>: Decomposition of perovskite into MnO and MnTi<sub>2</sub>O<sub>5</sub>. Phys. Chem. Miner. 38, 251-258
- 21. X. Wu et al., High-pressure behavior of perovskite: FeTiO<sub>3</sub> dissociation into (Fe<sub>1-5t</sub> Ti<sub>δ</sub>) O and Fe<sub>1+5</sub>Ti<sub>2-5</sub>O<sub>5</sub>, Phys. Rev. Lett. 103, 065503 (2009).
- 22. D. Nishio-Hamane et al., Decomposition of perovskite FeTiO<sub>3</sub> into wüstite Fe<sub>1-x</sub>Ti<sub>0.5x</sub>O and orthorhombic FeTi<sub>3</sub>O<sub>7</sub> at high pressure. Phys. Rev. B 82, 092103 (2010).
- 23. M. Akaogi et al., High-pressure high-temperature phase relations in FeTiO<sub>3</sub> up to 35 GPa and 1600 °C. Phys. Chem. Miner. 44, 63-73 (2017).
- 24. J. Hustoft et al., Equation of state of NaMgF3 postperovskite: Implication for the seismic velocity changes in the D" region. Geophys. Res. Lett. 35, L10309 (2008)
- 25. C. D. Martin et al., Phase transitions and compressibility of NaMgF<sub>3</sub> (Neighborite) in perovskite- and post-perovskite-related structures. Geophys. Res. Lett. 33, L11305
- 26. J. Lin, S. Zhang, W. Guan, G. Yang, Y. Ma, Gold with +4 and +6 oxidation states in AuF<sub>4</sub> and AuF<sub>6</sub>. J. Am. Chem. Soc. 140, 9545-9550 (2018).
- 27. M. H. Shahnas, R. N. Pysklywec, D. A. Yuen, Penetrative convection in super-Earth planets: Consequences of MgSiO<sub>3</sub> postperovskite dissociation transition and implications for super-Earth GJ 876 d. J. Geophys. Res. Planets 123, 2162-2177 (2018).
- 28. F. Coppari et al., Experimental evidence for a phase transition in magnesium oxide at exoplanet pressures. Nat. Geosci. 6, 926-929 (2013).
- 29. A. Kubo et al., Stability and equation of state of the post-perovskite phase in MgGeO<sub>3</sub> to 2 Mbar, Geophys, Res. Lett. 33, L12S12 (2006).
- 30. A. Kubo et al., Rietveld structure refinement of MgGeO<sub>3</sub> post-perovskite phase to 1 Mbar, Am. Mineral, 93, 965-976 (2008).
- 31. A. P. van den Berg, D. A. Yuen, K. Umemoto, M. H. G. Jacobs, R. M. Wentzcovitch, Mass-dependent dynamics of terrestrial exoplanets using ab initio mineral properties. Icarus 317, 412-426 (2019).
- 32. B. Grocholski et al., Stability of the MgSiO<sub>3</sub> analog NaMgF<sub>3</sub> and its implication for mantle structure in super-Earths. Geophys. Res. Lett. 37, L14204 (2010).
- Y. Zhao et al., Critical phenomena and phase transition of perovskite-NaMgF<sub>3</sub> perovskite. Part II. Phys. Earth Planet. Inter. 76, 17-34 (1993).
- 34. J. Chen et al., Crystal chemistry of NaMgF<sub>3</sub> perovskite at high pressure and temperature. Am. Mineral. 90, 1534-1539 (2005).

## **Supplementary Material**

## Phase transitions beyond post-perovskite in NaMgF<sub>3</sub> to 160 GPa.

R. Dutta<sup>1\*</sup>, E. Greenberg<sup>2</sup>, V. B. Prakapenka<sup>2</sup> and T. S. Duffy<sup>1</sup>

<sup>1</sup>Department of Geosciences, Princeton University, NJ 08544, USA. <sup>2</sup>Center for Advanced Radiation Sources, University of Chicago, Chicago, IL 60637, USA.

## S1. Comparison of structural parameters.

Table S1. Comparison of the structural parameters of post-perovskite (pPv) ABX<sub>3</sub> compounds (A = Mg, Na; B = Si, Mg and X = O, F) based on theoretical calculations (1, 2).

Parameter	MgSiO <sub>3</sub> pPv	NaMgF <sub>3</sub> pPv	
c/a	2.48	2.48	
b/a	3.27	3.13	
Ay	0.253	0.2515	
X1y	0.927	0.929	
X2y	0.363	0.3604	
X2z	0.441	0.4399	
A-X/B-X	1.17	1.16	
Poly A/B	2.08	2.03	
X2-B-X2 angle (Degrees)	93.4	94.4	
B-X1/B-X2	0.97	0.97	
Octahedral tilt (Degrees)	138	140	

a, b and c refer to unit cell parameters; Poly A/B is the ratio of AX<sub>8</sub> and BX<sub>6</sub> polyhedral volumes.

Atomic positions of pPv are: A  $(0, y, \frac{3}{4})$ , B (0, 0, 0), X1  $(0, y, \frac{3}{4})$  and X2 (0, y, z).

MgSiO<sub>3</sub> pPv: 120 GPa, 0 K (Tsuchiya et al., 2004, Ref (1)).

NaMgF<sub>3</sub> pPv: 30 GPa, 0 K (Umemoto and Wentzcovitch, 2006, Ref. (2)).

## S2a. Experimental Methodology

The starting sample was synthesized according to established procedures (3). Stoichiometric proportions of NaF and MgF<sub>2</sub> were ground in an agate mortar under acetone for 2 hours. The mixture was then pressed to form pellets which were sintered in covered alumina crucibles for 48 hours at 1023 K. The synthesized polycrystalline aggregate was then re-ground and characterized by x-ray diffraction and Raman spectroscopy. The x-ray diffraction data were fit to an orthorhombic perovskite structure with lattice parameters in good agreement with literature data.

The sample was mixed with 10 wt% gold which served as both the pressure calibrant and laser absorber. The sample + Au mixture was then pressed into  $\sim$  7-10- $\mu$ m thick pellets. Rhenium gaskets were pre-indented to  $\sim$ 20-25  $\mu$ m thickness and 20-100  $\mu$ m diameter holes were drilled to form the sample chamber. The sample disks were then loaded into symmetric diamond anvil cells with 75-200  $\mu$ m culet diamond anvils mounted on WC or cubic BN seats. In one experiment (Exp 2a), neon was loaded into the sample chamber as pressure-transmitting medium using the gas-loading system at the GeoSoilEnviroCARS sector of the Advanced Photon Source (APS).

Angle-dispersive x-ray diffraction was carried out at beamline 13-ID-D of the APS using a monochromatic x-ray beam ( $\lambda$  = 0.3344 Å) focused to dimensions of ~3 µm x 3 µm with Kirkpatrick-Baez mirrors. A two-dimensional CCD (Mar165) or a CdTe 1M Pilatus detector was used to collect the diffraction patterns. A lanthanum hexaboride (LaB<sub>6</sub>) standard was used to calibrate the detector position and orientation. High temperatures were attained by double-sided heating (4) with diode pumped fiber lasers with ~15 µm spot size (5). Temperatures were measured from both sides of the sample using spectroradiometry (6). The laser power incident on

each side were adjusted independently so that the temperature differences across the sample was typically less than 100 K. Pressures were determined using the (111) diffraction peak and the EOS of Au (7, 8).

The x-ray diffraction patterns were fit using background-subtracted Voigt line shapes. Lattice parameters were calculated by least-squares refinement of the fitted peak positions (9). LeBail refinements were carried out on selected patterns using the programs GSAS/EXPGUI (10). Structures based on density functional theory calculations were used as the starting model for the refinements (section S2b). The parameters for all the observed phases were initially refined separately and then simultaneously. The lattice parameters were refined first, followed by the profile function (pseudo-Voigt with Finger-Cox-Jephcoat asymmetry and Stephens anisotropic strain broadening) and finally the background (Chebyshev polynomial, 8 terms).

Table S2. Experimental conditions and observed phases.

Experiment	Pressure Range (GPa)	Peak Temperature (K)	Phase(s) present	
Exp 1	0 - 13	300	Pv	
Exp 1	40	300	pPv	
Exp 1	58 - 70	300	$pPv + Sb_2S_3$	
Exp 1	87	300	$\mathrm{Sb}_2\mathrm{S}_3$	
Exp 2a*	90	1810	Sb <sub>2</sub> S <sub>3</sub>	
Exp 2b	87	2710	NaMg <sub>2</sub> F <sub>5</sub> + NaF	
Exp 3	134	2590	NaMg <sub>2</sub> F <sub>5</sub> + NaF	
Exp 4	162	2260	MgF <sub>2</sub> + NaF	
Exp 5	150	2200	$MgF_2 + NaF$	

<sup>\*</sup>Ne used as a pressure transmitting medium.

All phases were retained upon quenching to ambient temperature.

## **S2b.** Computational Details

Theoretical calculations were performed to obtain values for the lattice parameters of the NaMg<sub>2</sub>F<sub>5</sub> and Sb<sub>2</sub>S<sub>3</sub>-type NaMgF<sub>3</sub> phases to be used as starting values in the least-squares refinements. The calculations were performed using the plane wave implementation of density functional theory (DFT) (11, 12) as implemented in the CASTEP (13) code. The exchange-correlation energies were treated using the local density approximation (LDA). We used a kinetic energy cutoff of 410 eV for the basis set. The Brillouin zone was sampled using a Monkhorst-Pack (14) 2x5x2 and 3x3x2 *k*-point grid for the Sb<sub>2</sub>S<sub>3</sub>-type NaMgF<sub>3</sub> and NaMg<sub>2</sub>F<sub>5</sub> respectively. Ultrasoft (15) pseudopotentials were used to treat the electron-ion interactions. The geometry optimizations were carried out using the Broyden-Fletcher-Goldfarb-Shanno (16) algorithm and were considered complete when the forces on atoms were less than 0.03 eV/Å and the energy change was less than 1 x 10<sup>-5</sup> eV/atom. Both atomic positions and lattice parameters were optimized at each pressure step.

# S3. NaMgF<sub>3</sub> Neighborite (Perovskite) and Post-Perovskite

Figure S1. X-ray diffraction pattern of NaMgF<sub>3</sub> at 13 GPa and room temperature. The ticks at the bottom indicate the expected peak positions of perovskite (Pv, Red), gold (yellow) and rhenium (blue). Peaks for perovskite are indicated by their Miller indices. The lattice parameters are a = 5.069 (5) Å, b = 5.355 (4) Å and c = 7.361 (4) Å.

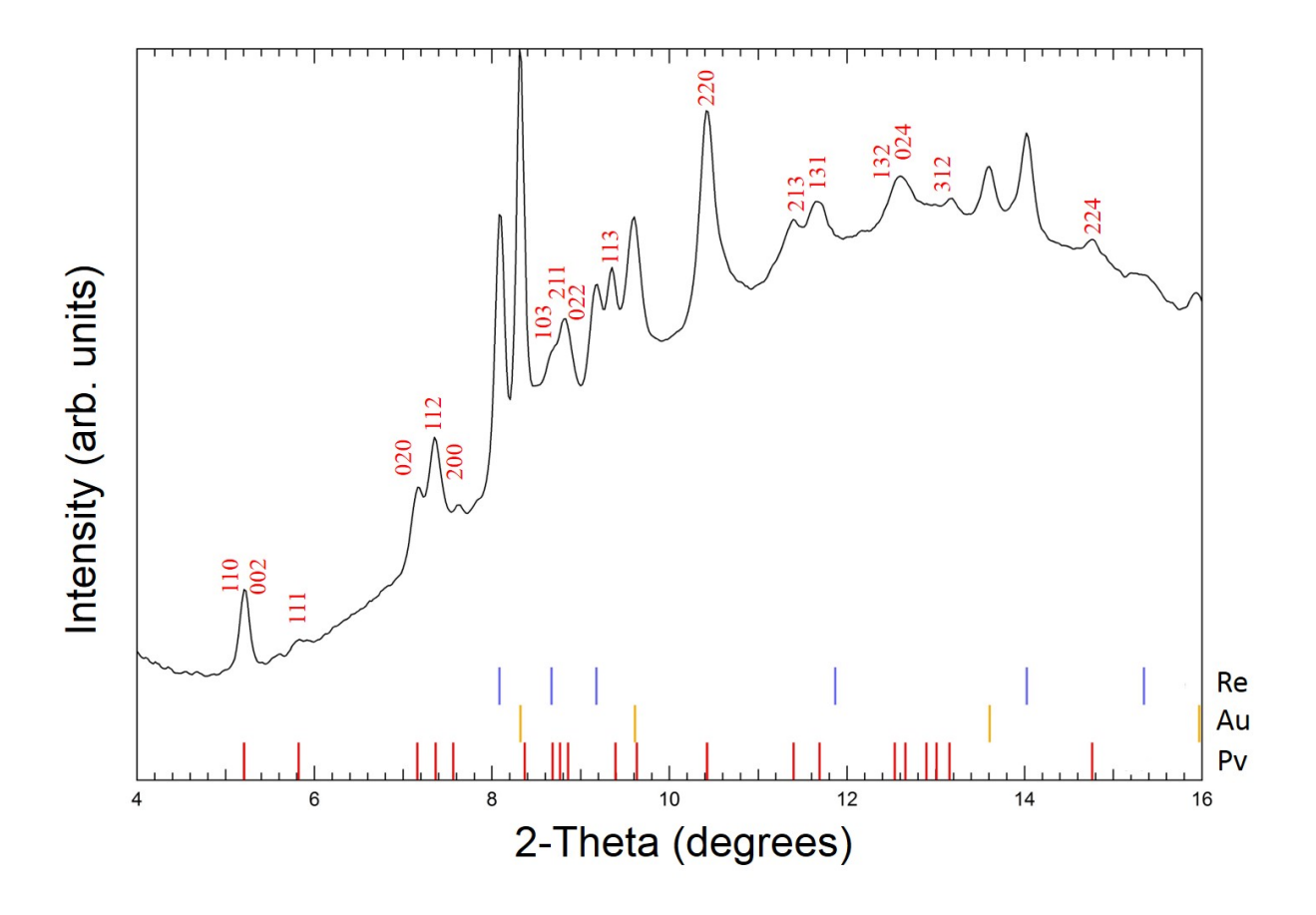
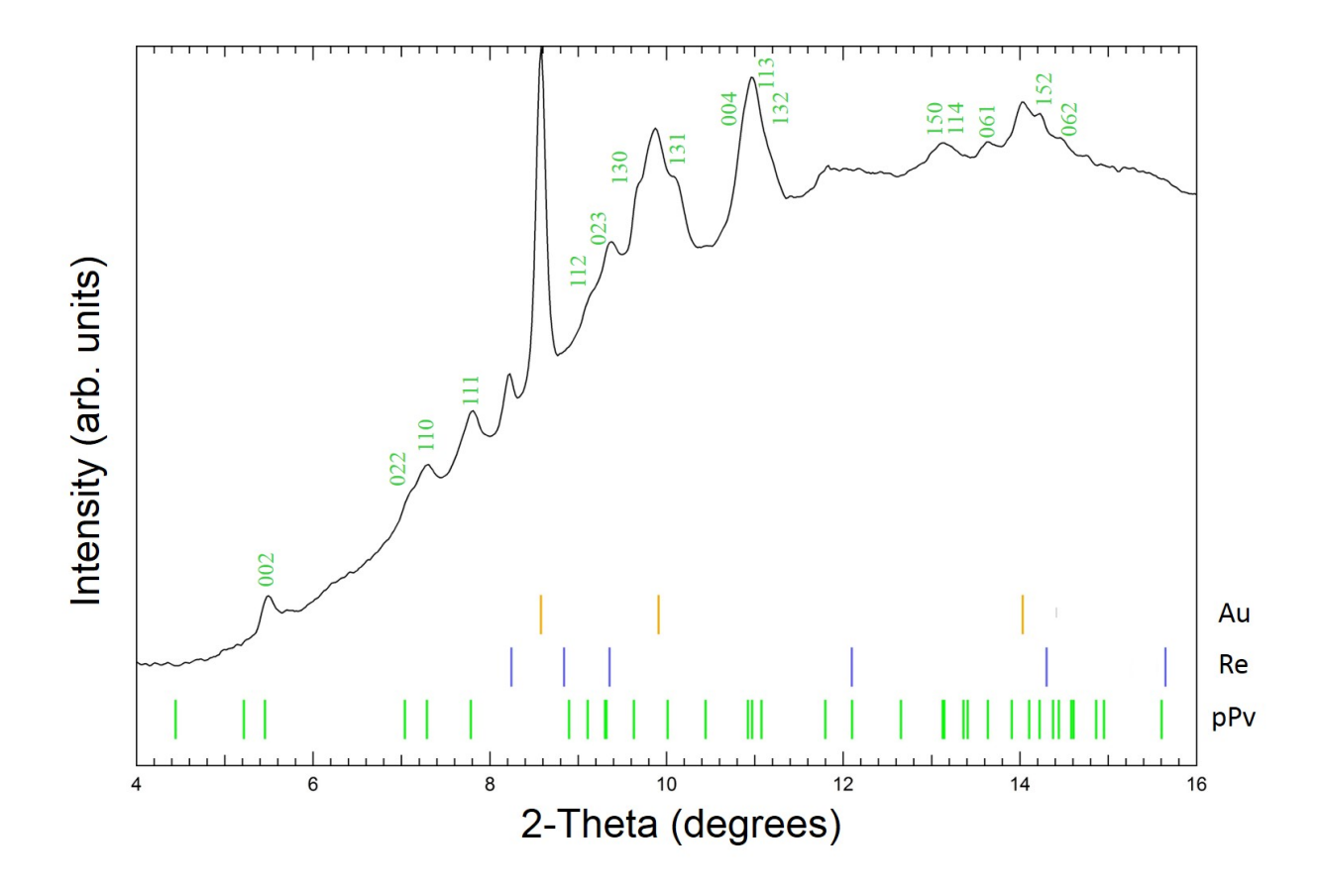


Figure S2. X-ray diffraction pattern for NaMgF<sub>3</sub> at 40 GPa (300 K). The ticks at the bottom indicate the calculated peak positions of post-perovskite (green), gold (yellow) and rhenium (blue). Post-perovskite peaks are labeled with their Miller indices. The unit cell dimensions are a = 2.761 (1) Å, b = 8.622 (3) Å and c = 7.026 (5) Å.



## S4. Sb<sub>2</sub>S<sub>3</sub>-type Phase

Figure S3. X-ray diffraction pattern of NaMgF<sub>3</sub> at 58 GPa and 300 K. The ticks at the bottom indicate the calculated peak positions of Sb<sub>2</sub>S<sub>3</sub>-type NaMgF<sub>3</sub> (purple), post-perovskite (green) and gold (yellow). The Miller indices of the Sb<sub>2</sub>S<sub>3</sub>-type (a = 7.276 (7) Å, b = 2.818 (2) Å and c = 7.282 (5) Å) and post-perovskite (a = 2.731 (2) Å, b = 8.322 (9) Å and c = 6.823 (3) Å) phases of NaMgF<sub>3</sub> are indicated.

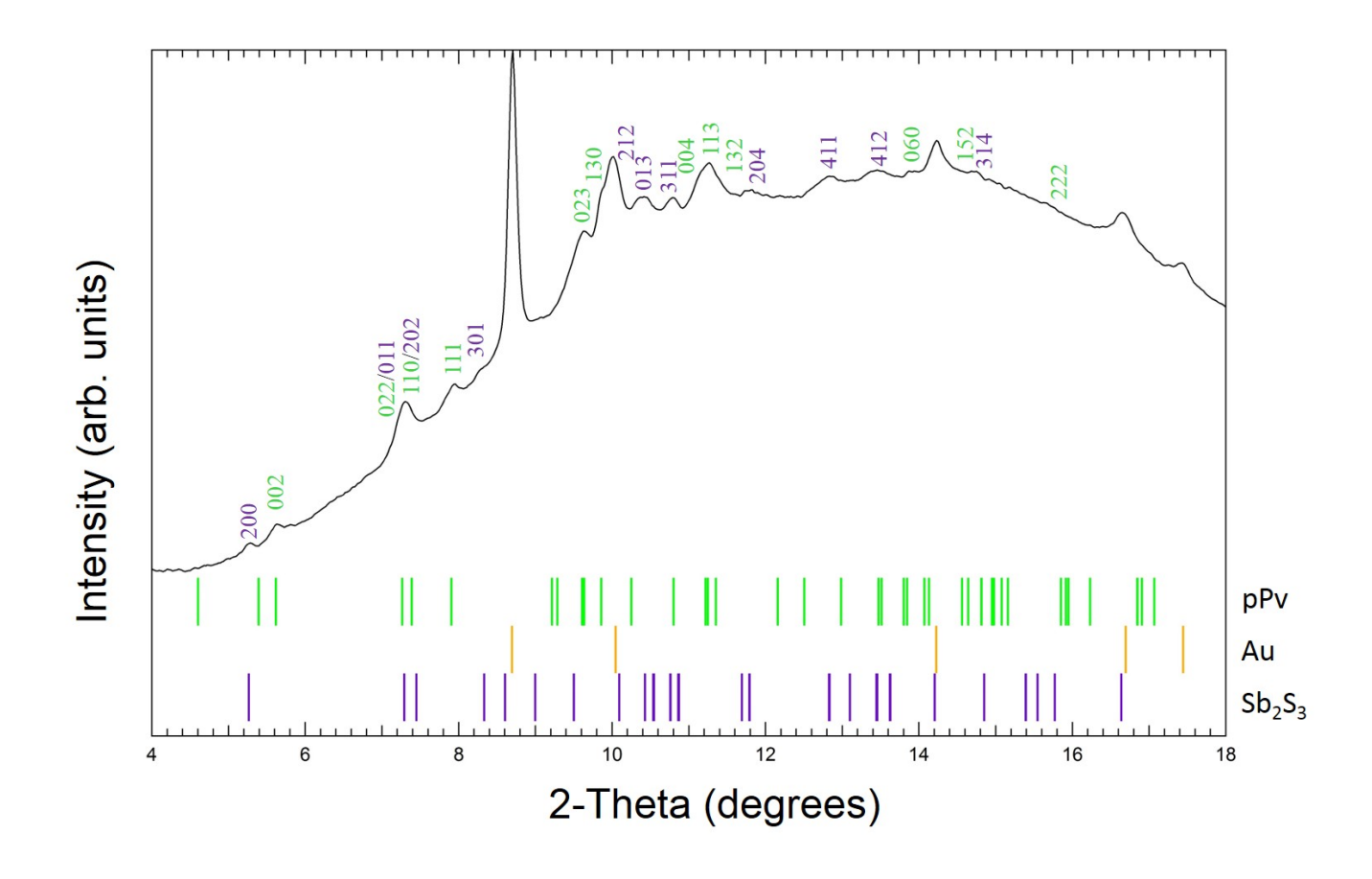


Figure S4. LeBail refinement of the diffraction pattern shown in Figure 2. The lattice parameters of the Sb<sub>2</sub>S<sub>3</sub>-type phase are a = 7.149 (2) Å, b = 2.716 (1) Å, and c = 7.065 (5) Å. The red, green and blue lines indicate the calculated pattern, background and the difference between the simulated and observed patterns, respectively. Peaks indicated by the star symbol were masked out in Figure 2 on textural grounds. Inset shows the caked diffraction pattern with orange circles indicating the spots give rising to the above-mentioned peaks.

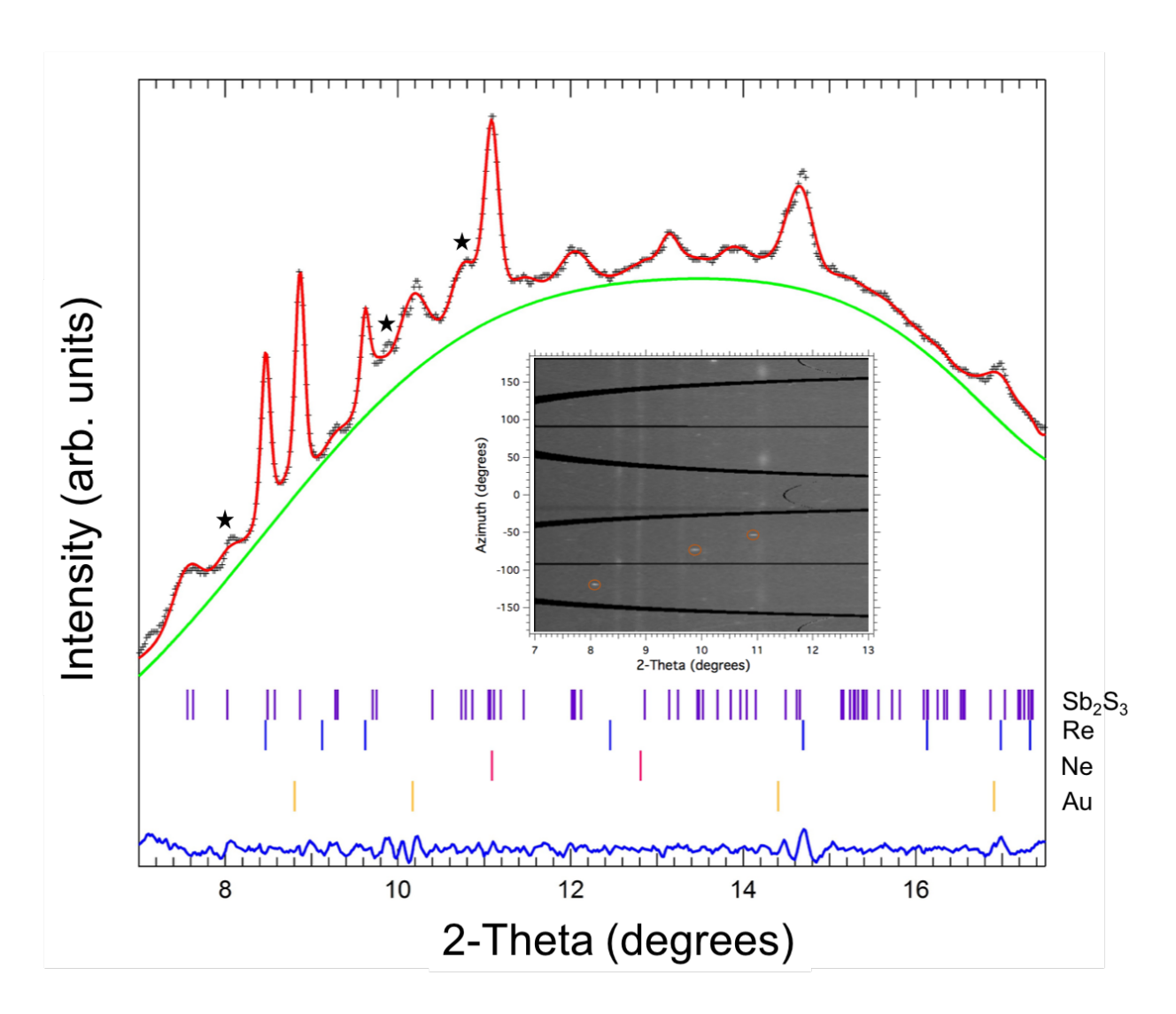


Figure S5. Lattice parameters of the Sb<sub>2</sub>S<sub>3</sub>-type phase as a function of pressure at 300 K. The pink datum represents the experiment where the sample was quenched from laser heating in a neon pressure medium. It should be noted that the *Pnma* setting has been adopted in this study for the Sb<sub>2</sub>S<sub>3</sub>-type phase [Pnma (a, b, c) = Pmcn (b, c, a)]. Solid lines are linear fits to the data.

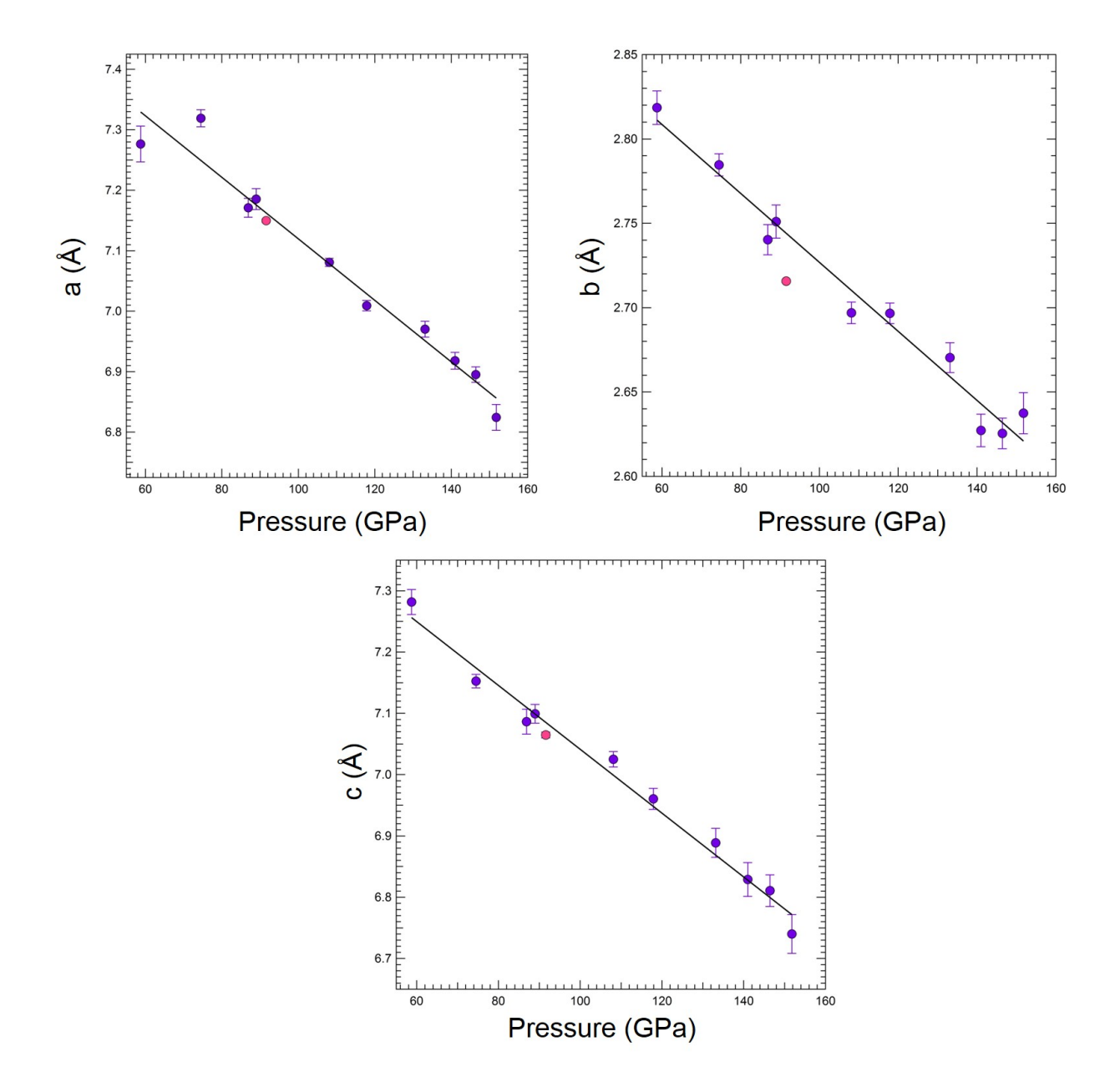


Table S3. Calculated and observed d-spacings of Sb<sub>2</sub>S<sub>3</sub>-type NaMgF<sub>3</sub> at 87 GPa (xrd pattern shown in inset of figure 2). The lattice parameters are a = 7.163 (4) Å, b = 2.741 (2) Å, c = 7.094 (4) Å.

h	k	l	$d_{ m obs}({ m \AA})$	$d_{ m calc}({ m \AA})$	$\Delta d$ (Å)
0	1	1	2.56250	2.55689	0.00561
1	1	2	2.07138	2.07585	-0.00447
0	1	3	1.78710	1.79048	-0.00338
1	1	3	1.73864	1.73704	0.00160
4	0	2	1.59860	1.59857	0.00003
1	1	4	1.45921	1.45784	0.00137

Since some of the assigned peaks (e.g. 113 and 311; 114 and 411) are closely spaced, peak assignments can be ambiguous. It should be noted that the a and c dimensions obtained from both experiments and theoretical calculations (2) (a = 7.296 Å and c = 7.289 Å at 50 GPa) are within 0.1% of each other. Thus, swapping the h and l indices does not significantly affect the results.

#### S5. $NaMg_2F_5 + NaF$

Two temperature-quenched x-ray diffraction patterns were obtained in experiment 2b (91 GPa) and 3 (137 GPa). The patterns are similar (accounting for differences in pressure) and so we discuss only one of them in detail here. Fig S6 shows diffraction patterns before and after heating at 134 GPa. We observe the presence of a strong peak at  $\sim$ 11.78° in the quenched pattern that is not present in the unheated one. This peak is consistent with the expected position of the strongest reflection (110) of NaF in the CsCl-type (B2) structure. That only a single NaF peak is observed in the spectrum is not surprising as all other peaks of the CsCl-type phase in the relevant 2 $\theta$  range are expected to have relative intensities of < 10% of the (110) peak.

The presence of NaF requires that another phase such as MgF<sub>2</sub> or NaMg<sub>2</sub>F<sub>5</sub> ( $P2_1/c$ ) must be present for chemical balance. The cotunnite-type phase of MgF<sub>2</sub> is expected to be stable above 64 GPa (17), but the observed diffraction peaks are not consistent with this phase. To examine the possible presence of NaMg<sub>2</sub>F<sub>5</sub>, we first optimized the structure at the required pressures using density functional theory calculations. The parameters reported in a computational study (18) at lower pressure (50 GPa) were used as the starting model for the optimization. The lattice parameters at 135 GPa obtained from our theoretical calculation (a = 5.454 Å, b = 4.780 Å, c = 7.408 Å and  $\beta = 89.89^{\circ}$ ) were then used to compare expected peak positions with the measured pattern. We found that the assemblage NaMg<sub>2</sub>F<sub>5</sub> + NaF can account for all the major peaks (some of which overlap with Sb<sub>2</sub>S<sub>3</sub>-type) in the pattern (Fig. S6). The lattice parameters obtained from least-squares fitting of our experimental data are in fair agreement with our calculated value at both 88 and 137 GPa. NaMg<sub>2</sub>F<sub>5</sub> + NaF thus provides the best fit to the current data (Tables S4 and S5).

We also examined whether our interpretation could be affected by the possible presence of diffraction peaks from the Re gasket. The observed peak at ~8.56° two-theta could potentially be assigned to the (002) peak from rhenium. However, we do not observe any evidence for the stronger Re peak (101) in the measured pattern or any evidence for Re at all in the unheated pattern recorded prior to heating. Examination of the two-dimensional CCD image shows that the diffraction ring at 8.56° does not show the characteristic hexagonal texture typical of the rhenium gasket reflection, but rather displays a spotty texture similar to other rings from the sample. This indicates that the presence of Re is not a viable explanation for this peak.

One other feature in the diffraction pattern that should be mentioned is the offset of the Au (111) and (200) peaks. The pressure determined from the Au (111) peak is 137 GPa but the corresponding pressure from the Au (200) peak is only 111 GPa. In terms of two-theta values, the expected position of Au (200) at 137 GPa is  $2\theta = 10.48^{\circ}$ , while the observed position is  $10.36^{\circ}$  ( $\Delta d = d_{expected} - d_{observed} = 0.02$  Å). This difference is larger than expected based on the expected strength of gold at this pressure. In FCC crystals, the presence of stacking faults (19) can cause the (111) and (200) peaks to shift in opposite directions i.e. (111) to higher angle and (200) to lower angle, with the (200) peak shifting more than (111). A combination of differential stress and stacking faults may be an explanation for the observed offset.

Figure S6. Observed x-ray diffraction pattern before (bottom) and after laser heating (top) to 2600 K at 134 GPa ( $in \ situ \ P = 137 \ GPa$ ). The predicted peak positions of gold (yellow) and NaMg<sub>2</sub>F<sub>5</sub> (brown) are shown at the bottom. Asterisk shows the position of the NaF (110) peak. Miller indices of the NaMg<sub>2</sub>F<sub>5</sub> phase are indicated next to the quenched xrd pattern.

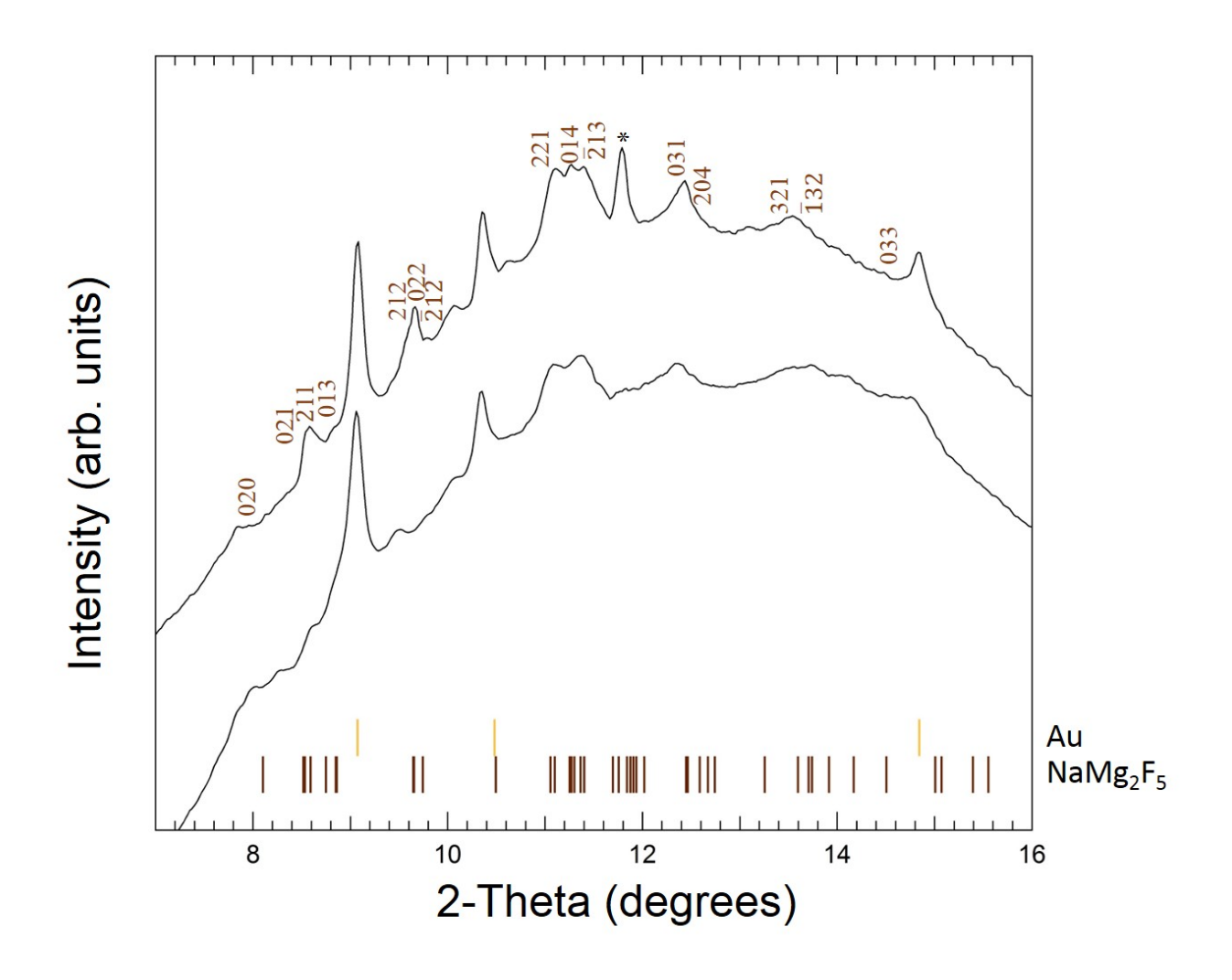


Table S4. Calculated and observed *d*-spacings of NaMg<sub>2</sub>F<sub>5</sub> at 88 GPa. The lattice parameters are a = 5.618 (3) Å, b = 4.977 (3) Å, c = 7.729 (7) Å and  $\beta = 89.23$  (9) degrees.

h	k	l	d <sub>obs</sub> (Å)	$d_{\mathrm{calc}}(\mathrm{\AA})$	Δd (Å)
0	1	3	2.28763	2.2879	-0.00026
2	1	2	2.07593	2.0778	-0.00188
2	2	1	1.81338	1.81442	-0.00104
0	2	3	1.78868	1.7898	-0.00112
0	3	1	1.62284	1.62195	0.00089
2	0	4	1.6029	1.60191	0.00099
-1	3	2	1.46938	1.46923	0.00015
4	0	0	1.40478	1.40449	0.00029

Table S5. Calculated and observed *d*-spacings of NaMg<sub>2</sub>F<sub>5</sub> at 137 GPa. The lattice parameters are a = 5.423 (16) Å, b = 4.732 (6) Å, c = 7.312 (13) Å and  $\beta = 89.2$  (2) degrees.

h	k	l	$d_{\mathrm{obs}}\left(\mathrm{\mathring{A}}\right)$	$d_{ m calc}( m \AA)$	$\Delta d$ (Å)
0	2	1	2.24533	2.25136	-0.00602
0	1	3	2.1698	2.16677	0.00303
2	1	2	1.99061	1.98851	0.0021
0	2	2	1.98377	1.9865	-0.00273
2	2	1	1.73316	1.73544	-0.00228
0	1	4	1.70389	1.70515	-0.00125
-2	1	3	1.68358	1.68314	0.00044
0	3	1	1.5454	1.54207	0.00334

## S5. NaF + MgF<sub>2</sub>

The major peaks in the diffraction pattern at 160 GPa shown in Fig. 4 can be attributed to cotunnite-type MgF<sub>2</sub> (Table S6), Au and CsCl-type NaF except for a peak marked with an asterisk in the figure ( $2\theta = 9.75^{\circ}$ , d = 1.97 Å). Fig. S7 shows diffraction patterns recorded at different temperatures during this heating cycle. The unexplained peak is absent in the room-temperature diffraction pattern before heating. It first appears in the pattern at ~1750 K, before the appearance of any evidence of peaks of the binary fluorides, which only appear at higher temperature (~1830 K). This observation suggests that the peak may be from a reaction product possibly involving carbon from the anvils which have been observed in other laser-heated DAC experiments (17) but its origin requires further investigation.

Alternatively, this peak could be from a gold fluoride. A recent theoretical study (20) proposed stable gold fluorides with variable oxidation states to be stable at high-pressure. Under pressures comparable to our experimental conditions, we find  $Au_2F$  (P4/nmm, a = 2.641 Å and c = 8.565 Å at 160 GPa) is broadly consistent with the concerned peak.

Figure S7. X-ray diffraction patterns of NaMgF<sub>3</sub> on heating at 162 GPa. The asterisk indicates the unexplained diffraction peak. In the upper three patterns, all other major peaks can be assigned to  $MgF_2 + NaF + Au$  (refer Fig. 4 for indexing). The red and blue arrows indicate the peak positions of  $MgF_2$  and NaF respectively. The lower two diffraction patterns can be indexed using  $Sb_2S_3$ -type  $NaMgF_3$ .

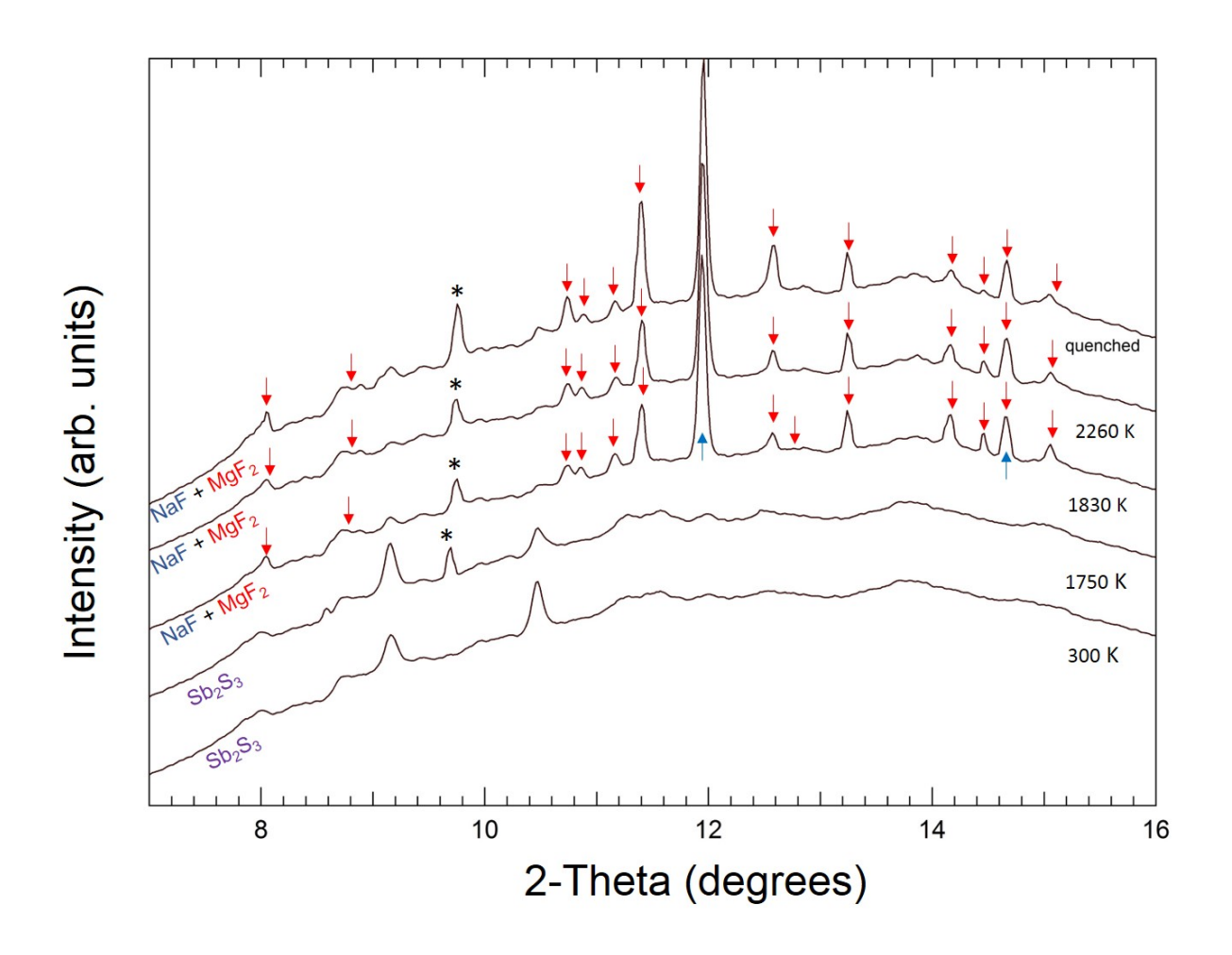


Table S6. Calculated and observed *d*-spacings of cotunnite-type MgF<sub>2</sub> at 160 GPa. The lattice parameters are a = 4.667 (2) Å, b = 2.704 (1) Å and c = 5.545 (1) Å.

h	k	l	$d_{ m obs}({ m \AA})$	$d_{ m calc}( m \AA)$	$\Delta d$ (Å)
1	0	2	2.38411	2.38382	0.00029
1	1	2	1.78722	1.78815	-0.00093
2	1	0	1.76692	1.76674	0.00018
1	0	3	1.71923	1.7186	0.00062
2	1	1	1.68342	1.68337	0.00005
0	1	3	1.52734	1.52598	0.00136
1	1	3	1.44967	1.45043	-0.00077
3	0	2	1.35685	1.35684	0.00001
1	0	4	1.32856	1.32897	-0.00041
3	1	1	1.3104	1.31036	0.00004

#### References

- 1. Tsuchiya T, Tsuchiya J, Umemoto K, Wentzcovitch RM (2004) Phase transition in MgSiO<sub>3</sub> perovskite in the earth's lower mantle. *Earth and Planetary Science Letters* 224(3):241–248.
- 2. Umemoto K, Wentzcovitch RM (2006) Potential ultrahigh pressure polymorphs of ABX<sub>3</sub>-type compounds. *Physical Review B* 74(22):224105.
- 3. Zhao Y, Weidner DJ, Parise JB, Cox DE (1993) Thermal expansion and structural distortion of perovskite data for NaMgF<sub>3</sub> perovskite. Part I. *Physics of the Earth and Planetary Interiors* 76(1–2):1–16.
- 4. Mao H, Shen G, Hemley RJ, Duffy TS (1998) X Ray diffraction with a double hot-plate laser-heated diamond cell. *Properties of Earth and Planetary Materials at High Pressure and Temperature* (American Geophysical Union), pp 27–34.
- 5. Prakapenka VB, et al. (2008) Advanced flat top laser heating system for high pressure research at GSECARS: application to the melting behavior of germanium. *High Pressure Research* 28(3):225–235.
- 6. Jephcoat AP, Besedin SP (1996) Temperature measurement and melting determination in the laser-heated diamond-anvil cell. *Philosophical Transactions: Mathematical, Physical and Engineering Sciences* 354(1711):1333–1360.
- 7. Dewaele A, Loubeyre P, Mezouar M (2004) Equations of state of six metals above 94 GPa. *Physical Review B* 70(9):094112.
- 8. Fei Y, et al. (2007) Toward an internally consistent pressure scale. *Proceedings of the National Academy of Sciences of the United States of America* 104(22):9182–9186.
- 9. Holland TJB, Redfern SAT (1997) Unit cell refinement from powder diffraction data; the use of regression diagnostics. *Mineralogical Magazine* 61(1):65–77.
- 10. Toby BH (2001) EXPGUI, a graphical user interface for GSAS. *Journal of Applied Crystallography* 34(2):210–213.
- 11. Hohenberg P, Kohn W (1964) Inhomogeneous electron gas. *Physical Review* 136(3B): B864–B871.
- 12. Kohn W, Sham LJ (1965) Self-consistent equations including exchange and correlation effects. *Physical Review* 140(4A): A1133–A1138.
- 13. Clark SJ, et al. (2009) First principles methods using CASTEP. *Zeitschrift für Kristallographie Crystalline Materials* 220(5/6):567–570.
- 14. Monkhorst HJ, Pack JD (1976) Special points for Brillouin-zone integrations. *Physical Review B* 13(12):5188–5192.

- 15. Vanderbilt D (1990) Soft self-consistent pseudopotentials in a generalized eigenvalue formalism. *Physical Review B* 41(11):7892–7895.
- 16. Broyden CG (1970) The convergence of a class of double-rank minimization algorithms 1. General considerations. *IMA Journal of Applied Math* 6(1):76–90.
- 17. Grocholski B, Shim S-H, Prakapenka VB (2010) Stability of the MgSiO<sub>3</sub> analog NaMgF<sub>3</sub> and its implication for mantle structure in super-Earths. *Geophysical Research Letters* 37(14): L14204.
- 18. Umemoto K, Wentzcovitch RM (2015) Two-stages dissociation of NaMgF<sub>3</sub> post-perovskite: a potential low-pressure analog of MgSiO<sub>3</sub> at multi-Mbar pressures. *JPS Conference Proceedings* 4:011002.
- 19. Makinson JD, et al. (2000) X-ray diffraction signatures of defects in nanocrystalline materials. *Advances in X-ray Analysis* 42:407–411.
- 20. Lin J, Zhang S, Guan W, Yang G, Ma Y (2018) Gold with +4 and +6 oxidation states in AuF<sub>4</sub> and AuF<sub>6</sub>. *Journal of American Chemical Society* 140(30):9545–9550.